

Binary Millisecond Pulsar Discovery via Gamma-Ray Pulsations

H. J. Pletsch^{1,2*}, L. Guillemot³, H. Fehrmann^{1,2}, B. Allen^{1,2,4}, M. Kramer^{3,5}, C. Aulbert^{1,2},
M. Ackermann⁶, M. Ajello⁷, A. de Angelis⁸, W. B. Atwood⁹, L. Baldini¹⁰, J. Ballet¹¹,
G. Barbiellini^{12,13}, D. Bastieri^{14,15}, K. Bechtol⁷, R. Bellazzini¹⁶, A. W. Borgland⁷,
E. Bottacini⁷, T. J. Brandt^{17,18}, J. Bregeon¹⁶, M. Brigida^{19,20}, P. Bruel²¹, R. Buehler⁷,
S. Buson^{14,15}, G. A. Caliendo²², R. A. Cameron⁷, P. A. Caraveo²³, J. M. Casandjian¹¹,
C. Cecchi^{24,25}, Ö. Çelik^{26,27,28}, E. Charles⁷, R.C.G. Chaves¹¹, C. C. Cheung²⁹,
J. Chiang⁷, S. Ciprini^{30,25}, R. Claus⁷, J. Cohen-Tanugi³¹, J. Conrad^{32,33}, S. Cutini³⁴,
F. D'Ammando^{24,35,36}, C. D. Dermer³⁷, S. W. Digel⁷, P. S. Drell⁷, A. Drlica-Wagner⁷,
R. Dubois⁷, D. Dumora³⁸, C. Favuzzi^{19,20}, E. C. Ferrara²⁶, A. Franckowiak⁷,
Y. Fukazawa³⁹, P. Fusco^{19,20}, F. Gargano²⁰, N. Gehrels²⁶, S. Germani^{24,25},
N. Giglietto^{19,20}, F. Giordano^{19,20}, M. Giroletti⁴⁰, G. Godfrey⁷, I. A. Grenier¹¹,
M.-H. Grondin^{41,42}, J. E. Grove³⁷, S. Guiriec²⁶, D. Hadasch²², Y. Hanabata³⁹,
A. K. Harding²⁶, P. R. den Hartog⁷, M. Hayashida^{7,43}, E. Hays²⁶, A. B. Hill^{7,44},
X. Hou⁴⁵, R. E. Hughes⁴⁶, G. Jóhannesson⁴⁷, M. S. Jackson^{48,33}, T. Jogler⁷,
A. S. Johnson⁷, W. N. Johnson³⁷, J. Kataoka⁴⁹, M. Kerr⁷, J. Knödseder^{17,18},
M. Kuss¹⁶, J. Lande⁷, S. Larsson^{32,33,50}, L. Latronico⁵¹, M. Lemoine-Goumard³⁸,
F. Longo^{12,13}, F. Loparco^{19,20}, M. N. Lovellette³⁷, P. Lubrano^{24,25}, F. Massaro⁷,
M. Mayer⁶, M. N. Mazziotta²⁰, J. E. McEnery^{26,52}, J. Mehault³¹, P. F. Michelson⁷,
W. Mitthumsiri⁷, T. Mizuno⁵³, M. E. Monzani⁷, A. Morselli⁵⁴, I. V. Moskalenko⁷,
S. Murgia⁷, T. Nakamori⁴⁹, R. Nemmen²⁶, E. Nuss³¹, M. Ohno⁵⁵, T. Ohsugi⁵³,
N. Omodei⁷, M. Orienti⁴⁰, E. Orlando⁷, F. de Palma^{19,20}, D. Paneque^{56,7},
J. S. Perkins^{26,28,27,57}, F. Piron³¹, G. Pivato¹⁵, T. A. Porter^{7,7}, S. Rainò^{19,20},
R. Rando^{14,15}, P. S. Ray³⁷, M. Razzano^{16,9}, A. Reimer^{58,7}, O. Reimer^{58,7}, T. Reposeur³⁸,
S. Ritz⁹, R. W. Romani⁷, C. Romoli¹⁵, D.A. Sanchez⁴¹, P. M. Saz Parkinson⁹,
A. Schulz⁶, C. Sgrò¹⁶, E. do Couto e Silva⁷, E. J. Siskind⁵⁹, D. A. Smith³⁸,
G. Spandre¹⁶, P. Spinelli^{19,20}, D. J. Suson⁶⁰, H. Takahashi³⁹, T. Tanaka⁷, J. B. Thayer⁷,
J. G. Thayer⁷, D. J. Thompson²⁶, L. Tibaldo^{14,15}, M. Tinivella¹⁶, E. Troja²⁶,
T. L. Usher⁷, J. Vandenbroucke⁷, V. Vasileiou³¹, G. Vianello^{7,61}, V. Vitale^{54,62},
A. P. Waite⁷, B. L. Winer⁴⁶, K. S. Wood³⁷, M. Wood⁷, Z. Yang^{32,33}, S. Zimmer^{32,33}

*To whom correspondence should be addressed. Email: holger.pletsch@aei.mpg.de

Affiliations are listed at the end of the paper.

Millisecond pulsars (MSPs), old neutron stars spun-up by accreting matter from a companion star, can reach high rotation rates of hundreds of revolutions per second. Until now, all such “recycled” rotation-powered pulsars have been detected by their spin-modulated radio emission. In a computing-intensive blind search of gamma-ray data from the Fermi Large Area Telescope (with partial constraints from optical data), we detected a 2.5-millisecond pulsar, PSR J1311–3430. This unambiguously explains a formerly unidentified gamma-ray source that had been a decade-long enigma, confirming previous conjectures. The pulsar is in a circular orbit with an orbital period of only 93 minutes, the shortest of any spin-powered pulsar binary ever found.

Almost exactly 30 years ago, radio observations detected the first neutron star with a millisecond spin period (1). Launched in 2008, the Large Area Telescope (LAT) on the Fermi Gamma-ray Space Telescope (2) confirmed that many radio-detected millisecond pulsars (MSPs) are also bright gamma-ray emitters (3). In each case, gamma-ray (0.1–100 GeV) pulsations were revealed by using rotation parameters obtained from radio telescopes (4) to assign rotational phases to LAT-detected photons.

The Fermi LAT also provides sufficient sensitivity to detect pulsars via direct searches for periodicity in the sparse gamma-ray photons. Such blind searches (5) of LAT data for solitary pulsars have so far unveiled 36 younger gamma-ray pulsars (6–9) with rotation rates between 2 and 20 Hz. In the radio band all but four of these objects remain completely undetected despite deep follow-up radio searches (10). This is a large fraction of all young gamma-ray emitting neutron stars and shows that such blind-search gamma-ray detections are essential for understanding the pulsar population (11). However, no MSP has been detected via gamma-ray pulsations until now, and so we have not been able to see if a similar population of radio-quiet MSPs exists.

The blind-search problem for gamma-ray pulsars is computationally demanding, because the relevant pulsar parameters are unknown a priori and must be explicitly searched. For observation times spanning several years, this requires a dense grid to cover the multi-dimensional parameter space, with a tremendous number of points to be individually tested. Blind searches for MSPs in gamma-ray data are vastly more difficult than for slower pulsars largely because the search must extend to much higher spin frequencies [to and beyond 716 Hz (*12*)]. Furthermore, most MSPs are in binary systems, where the additionally unknown orbital parameters can increase the computational complexity by orders of magnitude. Thus, blind searches for binary MSPs were hitherto virtually unfeasible.

We have now broken this impasse, detecting a binary MSP, denoted PSR J1311–3430, in a direct blind search of the formerly unidentified gamma-ray source 2FGL J1311.7–3429, one of the brightest listed in the Fermi-LAT Second Source Catalog [2FGL, (*13*)]. This source also had counterparts in several earlier gamma-ray catalogs and was first registered in data from the Energetic Gamma Ray Experiment Telescope [EGRET, (*14*)] on the Compton Gamma Ray Observatory.

In a search for potential optical counterparts of 2FGL J1311.7–3429, Romani (*15*) identified a quasi-sinusoidally modulated optical flux with a period of 93 minutes and conjectured this to be a “black-widow” pulsar binary system (*16*). In this interpretation, an MSP strongly irradiates what is left of the donor companion star to eventually evaporate it. This plausibly explained the observed brightness variation resulting from strong heating of one side of the companion by the pulsar radiation. Associating this optical variation with the orbital period of the putative binary system constrained the ranges of orbital search parameters and also confined the sky location for the search. Thus, these constraints made a blind binary-MSP search in LAT data feasible; however the computational challenge involved remained enormous. To test the binary-MSP hypothesis as the possible nature of 2FGL J1311.7–3429, we developed an advanced method

to search the LAT data for pulsations over the entire relevant parameter space.

Under the black-widow interpretation, the search is confined toward the sky location of the potential optical counterpart and the orbit is expected to be circular, leaving a five-dimensional search space. The individual dimensions are spin frequency f , its rate of change \dot{f} , the orbital period P_{orb} , time of ascending node T_{asc} , and $x = a_p \sin \iota$, the projection of the pulsar semi-major axis a_p onto the line of sight with orbital inclination angle ι . We designed the blind search to maintain sensitivity to very high pulsar spin frequencies $f < 1.4$ kHz, and values of \dot{f} typical for MSPs, $-5 \times 10^{-13} \text{ Hz s}^{-1} < \dot{f} < 0$. Although the optical data constrain P_{orb} and T_{asc} , the uncertainties are by far larger than the precision necessary for a pulsar detection. This required us to search ranges of $P_{\text{orb}} = 5626.0 \pm 0.1 \text{ s}$ and $T_{\text{asc}} = 56009.131 \pm 0.012 \text{ MJD}$ around the nominal values (15), and $0 < x < 0.1 \text{ lt-s}$ (light-seconds).

Searching this five-dimensional parameter space fully coherently given a multiple-year data time span is computationally impossible. To solve this problem, we used the hierarchical (three-staged) search strategy that previously enabled the detection of ten solitary, younger (i.e. non-MSP) pulsars in blind searches of LAT data (8, 9), exploiting methods originally developed to detect gravitational waves from pulsars (17–20). Here we expanded this approach to also search over binary orbital parameters. The first stage of the hierarchical scheme is the most computing-intensive and employs an efficient “semi-coherent” method (8), extending (21). This step involves (incoherently) combining coherent Fourier power computed using a window of 2^{20} s (~ 12 days) by sliding the window over the entire LAT data set (hence the term “semi-coherent”). In a second stage, significant semi-coherent candidates are automatically followed up through a fully coherent analysis made possible because only a small region of parameter space around the candidate is explored. A third stage further refines coherent pulsar candidates by including higher signal harmonics [using the H -test (22, 23)]. The computing cost to coherently follow up a single semi-coherent candidate is negligible compared to the total cost of the

first stage. Therefore, constructing the search grid of the semi-coherent stage as efficiently as possible is of utmost importance.

The key element in constructing an optimally efficient grid for the semi-coherent search is a distance metric on the search space (17–19, 24). The metric provides an analytic geometric tool measuring the expected fractional loss in signal-to-noise ratio (S/N) squared for any given pulsar-signal location at a nearby grid point. The metric is obtained by locally Taylor-expanding the fractional loss to second order around the parameter-space location of a given signal. In contrast to searching for solitary pulsars, a difficulty in the binary case is that the metric components explicitly depend upon the search parameters (24). Thus, the metric (and so the grid-point density required to not miss a signal) changes across orbital parameter space. Constructing a simple lattice with constant spacings would be highly inefficient, resulting in either vast over- or under-covering of large parameter-space regions. We developed a grid-construction algorithm (25) that effectively utilizes the metric formalism. Orbital grid points were first placed at random, then those that were either too close together or too far apart according to the metric were moved (barycentric shifts), minimizing the maximum possible loss in S/N for any pulsar signal across the entire search parameter space. By design the resulting grid (25) ensured never losing more than 30% in S/N for any signal parameters.

The input LAT data we prepared for this search spanned almost four years (1437 days) and includes gamma-ray photons with LAT-reconstructed directions within 15° around the targeted sky position (25). To improve the S/N of a putative pulsar signal, we assigned each photon a weight (23) measuring the probability of originating from the conjectured pulsar, computed with a spectral likelihood method (25). The gamma-ray spectrum of 2FGL J1311.7–3429 is best modeled by an exponentially cut-off power law (Fig. S1), with spectral parameters reminiscent of other gamma-ray pulsars (Table 1). The computational work of the search was done on the ATLAS cluster in Hannover, Germany. Soon after initiation, the searching procedure

convincingly detected PSR J1311–3430.

Following the blind-search detection, we refined the pulsar parameters further in a timing analysis (26). We obtained pulse times of arrival (TOAs) from subdividing the LAT data into 40 segments of about equal length. We produced a pulse profile for each segment using the initial pulsar parameters, and cross-correlated each pulse profile with a multi-Gaussian template derived from fitting the entire data set to determine the TOAs. We used the Tempo2 software (27) to fit the TOAs to a timing model including sky position, f , \dot{f} , and binary-orbit parameters (Fig. 1 and Table 1). We found no statistically significant evidence for orbital eccentricity at the $e < 10^{-3}$ level. We measured a marginal evidence for a total proper motion of $8 \pm 3 \text{ mas yr}^{-1}$. Generally, the observed value of $\dot{f} = -3.198(2) \times 10^{-15} \text{ Hz s}^{-1}$ is only an upper limit of the intrinsic frequency change \dot{f}_{in} , because of the Shklovskii effect in which Doppler shifts caused by the proper motion can account for part of \dot{f} . Assuming the proper motion of PSR J1311–3430 is small enough to approximate $\dot{f} \cong \dot{f}_{\text{in}}$, we derived further quantities from the pulsar rotational parameters (Table 1).

The rotational ephemeris of PSR J1311–3430 also provides constraints on the companion mass m_c through the binary mass function that combines x , P_{orb} , and the gravitational constant G ,

$$\begin{aligned} f(m_p, m_c) &= \frac{4\pi^2}{G} \frac{x^3}{P_{\text{orb}}^2} = \frac{(m_c \sin \iota)^3}{(m_c + m_p)^2} \\ &= 2.995(3) \times 10^{-7} \text{M}_{\odot} \end{aligned} \quad (1)$$

where m_p is the pulsar mass and M_{\odot} the mass of the Sun. Typical MSP masses are $1.35 - 2.0 \text{ M}_{\odot}$. Assuming $m_p = 1.35 \text{ M}_{\odot}$ and $\iota = 90^\circ$ (orbit is edge-on) yields the minimum companion mass, $m_c > 8.2 \times 10^{-3} \text{ M}_{\odot}$, which is only about eight times higher than the mass of Jupiter. By means of Kepler’s third law and typical MSP masses ($m_p \gg m_c$), the binary separation, $a = a_p + a_c$, is accurately approximated by $a = 0.75 \text{ R}_{\odot} (m_p / 1.35 \text{ M}_{\odot})^{1/3}$, where R_{\odot} is the

radius of the Sun. Thus PSR J1311–3430 is likely the most compact pulsar binary known.

The compact orbit and the optical flaring events (15) suggest that the pulsar heating is driving a strong, possibly variable, stellar wind of ablated material of the companion. Interactions with the companion wind could affect the gamma-ray flux observed. In a dedicated analysis (25), we found no evidence for a modulation at the orbital period of the gamma-ray flux or its spectrum.

We also examined the gamma-ray spectral parameters of PSR J1311–3430 as a function of rotational phase (25). Dividing the data into ten segments according to different rotational-phase intervals, we spectrally analyzed each segment separately. In line with the background estimation in the pulse profile (Fig. 1), we detected significant gamma-ray emission at all phases. The gamma-ray spectrum in the off-pulse phase interval (Fig. S2) is better modeled by a cut-off power law, potentially indicative of magnetospheric origin from the pulsar, rather than by a simple power law which would more likely suggest intrabinary wind shock emission.

Repeated, sensitive radio searches of the previously unidentified gamma-ray source, including Green Bank Telescope (GBT) observations at 820 MHz gave no pulsar detection (28). However, material ablated from the companion by the pulsar irradiation might obscure radio pulses. At higher radio frequencies decreased scattering and absorption resulting in shorter eclipses is observed for other black-widow pulsars (12).

The optical observations provide evidence for strong heating of the pulsar companion that is near filling its Roche lobe (15). With $m_p = 1.35 M_\odot$ and $\iota = 90^\circ$ the Roche lobe radius of the companion is to good approximation (29) $R_L = 0.063 R_\odot$. The minimum mean density of the Roche-lobe filling companion directly follows from the orbital period (30), $\bar{\rho} = 45 \text{ g cm}^{-3}$. This is twice the density of the planetary-mass companion of PSR J1719–1438 (31). One scenario for the formation of that system posits an ultra-compact X-ray binary with a He or C degenerate donor transferring mass to the neutron star. However (32) argue that angular momentum

losses through gravitational-wave emission are insufficient to reach the low masses and short period of the PSR J1719–1438 system in the age of the Universe. Instead, strong heating to bloat the companion or extra angular momentum loss from a companion evaporative wind are required. An alternative scenario (33) proposes that a combination of angular momentum loss and wind evaporation from an initial companion mass of $2M_{\odot}$ in a 0.8 day orbit can bring the system to low masses and short orbital periods in ~ 6 Gyr. Indeed, their scenario produces a good match to the $m_c \sim 0.01M_{\odot}$, $P_{\text{orb}} \sim 0.065$ days seen for PSR J1311–3430. At this point in the evolution the system is detached, the companion is He-dominated and irradiation has taken over the evolution. Presumably continued irradiation can drive the system towards PSR J1719–1438-type companion masses, or produce an isolated MSP.

The direct detection of an MSP in a blind search of gamma-ray data implies that further MSPs, including other extreme binary pulsars, may exist among the bright, as-yet unidentified 2FGL gamma-ray sources [e.g. (34, 35)] which are too radio faint or obscured by dense companion winds to be found in typical radio searches.

References and Notes

1. D. C. Backer, S. R. Kulkarni, C. Heiles, M. M. Davis, W. M. Goss, *Nature* **300**, 615 (1982).
2. W. B. Atwood, *et al.*, *Astrophys. J.* **697**, 1071 (2009).
3. A. A. Abdo, *et al.*, *Science* **325**, 848 (2009).
4. D. A. Smith, *et al.*, *Astron. & Astrophys.* **492**, 923 (2008).
5. The term “blind search” is used to reflect the fact that the pulsar parameters are unknown a priori, implying that a wide range of pulsar parameters must be explicitly searched.
6. A. A. Abdo, *et al.*, *Science* **325**, 840 (2009).

7. P. M. Saz Parkinson, *et al.*, *Astrophys. J.* **725**, 571 (2010).
8. H. J. Pletsch, *et al.*, *Astrophys. J.* **744**, 105 (2012).
9. H. J. Pletsch, *et al.*, *Astrophys. J. Lett.* **755**, L12 (2012).
10. P. S. Ray, *et al.*, *arXiv:1205.3089* (2012).
11. K. P. Watters, R. W. Romani, *Astrophys. J.* **727**, 123 (2011).
12. J. W. T. Hessels, *et al.*, *Science* **311**, 1901 (2006).
13. P. L. Nolan, *et al.*, *Astrophys. J. Supp.* **199**, 31 (2012).
14. C. E. Fichtel, *et al.*, *Astrophys. J. Supp.* **94**, 551 (1994).
15. R. W. Romani, *Astrophys. J. Lett.* **754**, L25 (2012).
16. A. S. Fruchter, D. R. Stinebring, J. H. Taylor, *Nature* **333**, 237 (1988).
17. P. R. Brady, T. Creighton, *Phys. Rev. D* **61**, 082001 (2000).
18. H. J. Pletsch, B. Allen, *Phys. Rev. Lett.* **103**, 181102 (2009).
19. H. J. Pletsch, *Phys. Rev. D* **82**, 042002 (2010).
20. H. J. Pletsch, *Phys. Rev. D* **83**, 122003 (2011).
21. W. B. Atwood, M. Ziegler, R. P. Johnson, B. M. Baughman, *Astrophys. J. Lett.* **652**, L49 (2006).
22. O. C. de Jager, B. C. Raubenheimer, J. W. H. Swanepoel, *Astron. & Astrophys.* **221**, 180 (1989).
23. M. Kerr, *Astrophys. J.* **732**, 38 (2011).

24. C. Messenger, *Phys. Rev. D* **84**, 083003 (2011).
25. See supporting material on *Science* Online.
26. P. S. Ray, *et al.*, *Astrophys. J. Supp.* **194**, 17 (2011).
27. G. B. Hobbs, R. T. Edwards, R. N. Manchester, *Mon. Not. R. Astron. Soc.* **369**, 655 (2006).
28. S. M. Ransom, *et al.*, *Astrophys. J. Lett.* **727**, L16 (2011).
29. B. Paczyński, *Annu. Rev. Astron. Astrophys.* **9**, 183 (1971).
30. J. Frank, A. R. King, D. J. Raines, *Accretion Power in Astrophysics* (Cambridge Univ. Press, Cambridge, 1985).
31. M. Bailes, *et al.*, *Science* **333**, 1717 (2011).
32. L. M. van Haaften, G. Nelemans, R. Voss, P. G. Jonker, *Astron. & Astrophys.* **541**, A22 (2012).
33. O. G. Benvenuto, M. A. De Vito, J. E. Horvath, *Astrophys. J. Lett.* **753**, L33 (2012).
34. R. W. Romani, M. S. Shaw, *Astrophys. J. Lett.* **743**, L26 (2011).
35. M. Ackermann, *et al.*, *Astrophys. J.* **753**, 83 (2012).
36. A. A. Abdo, *et al.*, *Astrophys. J.* **713**, 154 (2010).
37. M. Ackermann, *et al.*, *Astrophys. J.* **726**, 35 (2011).
38. I. W. Harry, B. Allen, B. S. Sathyaprakash, *Phys. Rev. D* **80**, 104014 (2009).

Acknowledgments: This work was supported by the Max-Planck-Gesellschaft. The Fermi LAT Collaboration acknowledges support from several agencies and institutes for both development and the operation of the LAT as well as scientific data analysis. These include NASA and DOE in the United States, CEA/Irfu and IN2P3/CNRS in France, ASI and INFN in Italy, MEXT, KEK, and JAXA in Japan, and the K. A. Wallenberg Foundation, the Swedish Research Council and the National Space Board in Sweden. Additional support from INAF in Italy and CNES in France for science analysis during the operations phase is also gratefully acknowledged. Fermi LAT data are available from the Fermi Science Support Center (<http://fermi.gsfc.nasa.gov/ssc/>).

Received for publication 20 August 2012.

Accepted for publication 17 October 2012.

Published online 25 October 2012.

DOI: [10.1126/science.1229054](https://doi.org/10.1126/science.1229054)

Table 1. Measured and derived parameters for PSR J1311–3430. Numbers in parentheses are formal 1σ uncertainties in the last digits. Spectral parameters are averages over pulse phase. dd, days; hh, hours; mm, minutes; ss, seconds; MJD, Modified Julian Day.

Parameter	Value
Right ascension (J2000.0) (hh:mm:ss)	13:11:45.7242(2)
Declination (J2000.0) (dd:mm:ss)	−34:30:30.350(4)
Spin frequency, f (Hz)	390.56839326407(4)
Frequency derivative, \dot{f} (Hz s $^{-1}$)	−3.198(2) $\times 10^{-15}$
Reference time scale	TDB
Reference time (MJD)	55266.90789575858
Orbital period P_{orb} (d)	0.0651157335(7)
Projected pulsar semi-major axis x (lt-s)	0.010581(4)
Time of ascending node T_{asc} (MJD)	56009.129454(7)
Eccentricity e	< 0.001
Data span (MJD)	54682 - 56119
Weighted RMS residual (μ s)	17
<i>Derived Quantities</i>	
Companion mass m_c (M_{\odot})	> 0.0082
Spin-down luminosity \dot{E} (erg s $^{-1}$)	4.9×10^{34}
Characteristic age τ_c (yr)	1.9×10^9
Surface magnetic field B_S (G)	2.3×10^8
<i>Gamma-Ray Spectral Parameters</i>	
Photon index, Γ	1.8 ± 0.1
Cutoff energy, E_c (GeV)	3.2 ± 0.4
Photon flux above 0.1 GeV, F (10^{-8} photons cm $^{-2}$ s $^{-1}$)	9.2 ± 0.5
Energy flux above 0.1 GeV, G (10^{-11} erg cm $^{-2}$ s $^{-1}$)	6.2 ± 0.2

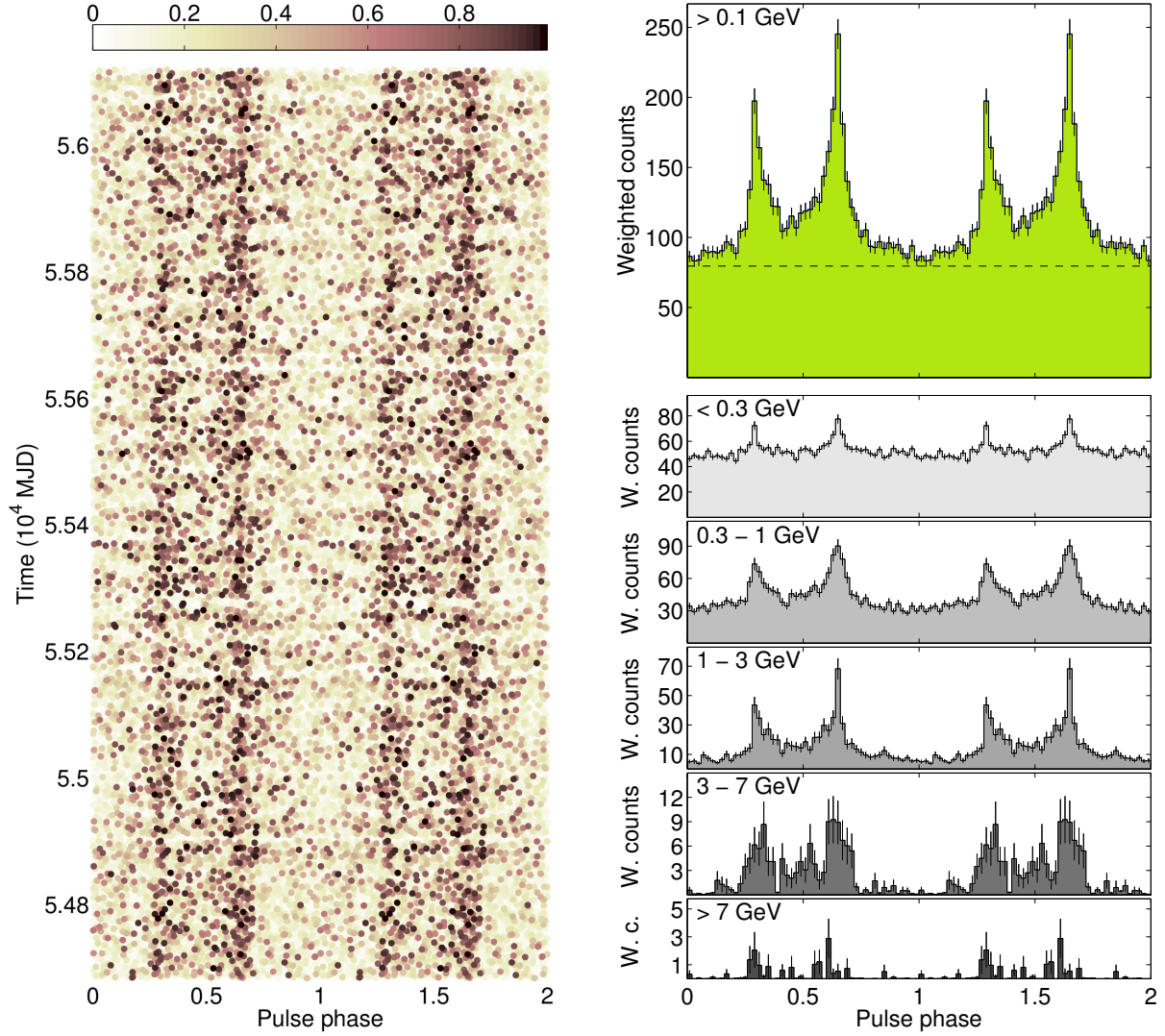


Fig. 1. Phase-time diagram and gamma-ray pulse profiles for PSR J1311–3430. Two pulsar rotations shown for clarity. **(Left)** The pulsar rotational phase for each gamma-ray-photon arrival time with the probability weight shown in color code. **(Right)** The pulse profiles in different energy bands. Each bin is 0.02 in phase and photon weights are used. The dashed line indicates the estimated background level from a surrounding annular region.

Affiliations:

- ¹ Max-Planck-Institut für Gravitationsphysik (Albert-Einstein-Institut), D-30167 Hannover, Germany
- ² Institut für Gravitationsphysik, Leibniz Universität Hannover, D-30167 Hannover, Germany
- ³ Max-Planck-Institut für Radioastronomie, Auf dem Hügel 69, D-53121 Bonn, Germany
- ⁴ Department of Physics, University of Wisconsin-Milwaukee, P.O. Box 413, Milwaukee, WI 53201, USA
- ⁵ Jodrell Bank Centre for Astrophysics, School of Physics and Astronomy, The University of Manchester, Manchester M13 9PL, UK
- ⁶ Deutsches Elektronen Synchrotron DESY, D-15738 Zeuthen, Germany
- ⁷ W. W. Hansen Experimental Physics Laboratory, Kavli Institute for Particle Astrophysics and Cosmology, Department of Physics and SLAC National Accelerator Laboratory, Stanford University, Stanford, CA 94305, USA
- ⁸ Dipartimento di Fisica, Università di Udine and Istituto Nazionale di Fisica Nucleare, Sezione di Trieste, Gruppo Collegato di Udine, I-33100 Udine, Italy
- ⁹ Santa Cruz Institute for Particle Physics, Department of Physics and Department of Astronomy and Astrophysics, University of California at Santa Cruz, Santa Cruz, CA 95064, USA
- ¹⁰ Università di Pisa and Istituto Nazionale di Fisica Nucleare, Sezione di Pisa I-56127 Pisa, Italy
- ¹¹ Laboratoire AIM, CEA-IRFU/CNRS/Université Paris Diderot, Service d'Astrophysique, CEA Saclay, F-91191 Gif sur Yvette, France
- ¹² Istituto Nazionale di Fisica Nucleare, Sezione di Trieste, I-34127 Trieste, Italy
- ¹³ Dipartimento di Fisica, Università di Trieste, I-34127 Trieste, Italy
- ¹⁴ Istituto Nazionale di Fisica Nucleare, Sezione di Padova, I-35131 Padova, Italy
- ¹⁵ Dipartimento di Fisica e Astronomia "G. Galilei", Università di Padova, I-35131 Padova, Italy
- ¹⁶ Istituto Nazionale di Fisica Nucleare, Sezione di Pisa, I-56127 Pisa, Italy
- ¹⁷ CNRS, IRAP, F-31028 Toulouse cedex 4, France
- ¹⁸ GAHEC, Université de Toulouse, UPS-OMP, IRAP, Toulouse, France
- ¹⁹ Dipartimento di Fisica "M. Merlin" dell'Università e del Politecnico di Bari, I-70126 Bari, Italy
- ²⁰ Istituto Nazionale di Fisica Nucleare, Sezione di Bari, I-70126 Bari, Italy
- ²¹ Laboratoire Leprince-Ringuet, École polytechnique, CNRS/IN2P3, Palaiseau, France
- ²² Institut de Ciències de l'Espai (IEEE-CSIC), Campus UAB, 08193 Barcelona, Spain
- ²³ INAF-Istituto di Astrofisica Spaziale e Fisica Cosmica, I-20133 Milano, Italy
- ²⁴ Istituto Nazionale di Fisica Nucleare, Sezione di Perugia, I-06123 Perugia, Italy
- ²⁵ Dipartimento di Fisica, Università degli Studi di Perugia, I-06123 Perugia, Italy
- ²⁶ NASA Goddard Space Flight Center, Greenbelt, MD 20771, USA
- ²⁷ Center for Research and Exploration in Space Science and Technology (CRESST) and NASA Goddard Space Flight Center, Greenbelt, MD 20771, USA
- ²⁸ Department of Physics and Center for Space Sciences and Technology, University of Maryland Baltimore County, Baltimore, MD 21250, USA
- ²⁹ National Research Council Research Associate, National Academy of Sciences, Washington, DC 20001, resident at Naval Research Laboratory, Washington, DC 20375, USA
- ³⁰ ASI Science Data Center, I-00044 Frascati (Roma), Italy
- ³¹ Laboratoire Univers et Particules de Montpellier, Université Montpellier 2, CNRS/IN2P3, Montpellier, France
- ³² Department of Physics, Stockholm University, AlbaNova, SE-106 91 Stockholm, Sweden
- ³³ The Oskar Klein Centre for Cosmoparticle Physics, AlbaNova, SE-106 91 Stockholm, Sweden
- ³⁴ Agenzia Spaziale Italiana (ASI) Science Data Center, I-00044 Frascati (Roma), Italy
- ³⁵ IASF Palermo, I-90146 Palermo, Italy
- ³⁶ INAF-Istituto di Astrofisica Spaziale e Fisica Cosmica, I-00133 Roma, Italy
- ³⁷ Space Science Division, Naval Research Laboratory, Washington, DC 20375-5352, USA
- ³⁸ Université Bordeaux 1, CNRS/IN2p3, Centre d'Études Nucléaires de Bordeaux Gradignan, F-33175 Gradignan, France

- ³⁹ Department of Physical Sciences, Hiroshima University, Higashi-Hiroshima, Hiroshima 739-8526, Japan
- ⁴⁰ INAF Istituto di Radioastronomia, I-40129 Bologna, Italy
- ⁴¹ Max-Planck-Institut für Kernphysik, D-69029 Heidelberg, Germany
- ⁴² Landessternwarte, Universität Heidelberg, Königstuhl, D-69117 Heidelberg, Germany
- ⁴³ Department of Astronomy, Graduate School of Science, Kyoto University, Sakyo-ku, Kyoto 606-8502, Japan
- ⁴⁴ School of Physics and Astronomy, University of Southampton, Highfield, Southampton, SO17 1BJ, UK
- ⁴⁵ Centre d'Études Nucléaires de Bordeaux Gradignan, IN2P3/CNRS, Université Bordeaux 1, BP120, F-33175 Gradignan Cedex, France
- ⁴⁶ Department of Physics, Center for Cosmology and Astro-Particle Physics, The Ohio State University, Columbus, OH 43210, USA
- ⁴⁷ Science Institute, University of Iceland, IS-107 Reykjavik, Iceland
- ⁴⁸ Department of Physics, Royal Institute of Technology (KTH), AlbaNova, SE-106 91 Stockholm, Sweden
- ⁴⁹ Research Institute for Science and Engineering, Waseda University, 3-4-1, Okubo, Shinjuku, Tokyo 169-8555, Japan
- ⁵⁰ Department of Astronomy, Stockholm University, SE-106 91 Stockholm, Sweden
- ⁵¹ Istituto Nazionale di Fisica Nucleare, Sezione di Torino, I-10125 Torino, Italy
- ⁵² Department of Physics and Department of Astronomy, University of Maryland, College Park, MD 20742, USA
- ⁵³ Hiroshima Astrophysical Science Center, Hiroshima University, Higashi-Hiroshima, Hiroshima 739-8526, Japan
- ⁵⁴ Istituto Nazionale di Fisica Nucleare, Sezione di Roma “Tor Vergata”, I-00133 Roma, Italy
- ⁵⁵ Institute of Space and Astronautical Science, JAXA, 3-1-1 Yoshinodai, Chuo-ku, Sagamihara, Kanagawa 252-5210, Japan
- ⁵⁶ Max-Planck-Institut für Physik, D-80805 München, Germany
- ⁵⁷ Harvard-Smithsonian Center for Astrophysics, Cambridge, MA 02138, USA
- ⁵⁸ Institut für Astro- und Teilchenphysik and Institut für Theoretische Physik, Leopold-Franzens-Universität Innsbruck, A-6020 Innsbruck, Austria
- ⁵⁹ NYCB Real-Time Computing Inc., Lattingtown, NY 11560-1025, USA
- ⁶⁰ Department of Chemistry and Physics, Purdue University Calumet, Hammond, IN 46323-2094, USA
- ⁶¹ Consorzio Interuniversitario per la Fisica Spaziale (CIFS), I-10133 Torino, Italy
- ⁶² Dipartimento di Fisica, Università di Roma “Tor Vergata”, I-00133 Roma, Italy

Supporting Online Material

Materials and Methods: Fermi-LAT Data Analysis

LAT data selection

The LAT surveys the entire sky every 3 hours (two orbits). In this work, we used data taken in this sky-survey mode between 4 August 2008 and 10 July 2012. The data were processed using the Fermi Science Tools¹ (v9r28p0). We selected gamma-ray photons belonging to the “Source” class under the P7V6 event selections. Photons with reconstructed zenith angles larger than 100° were rejected in order to exclude the bright contribution from the Earth’s limb. We also rejected photons recorded when the instrument was not operating in sky-survey mode, or when its rocking angle exceeded 52° . Finally, we selected only photons with energies > 0.1 GeV and found within 15° of the direction of the pulsar.

LAT data spectral analysis

We determined the gamma-ray spectral properties of PSR J1311–3430 by performing a binned likelihood analysis of this data set, using the `pyLikelihood` tool. The Galactic diffuse emission was modeled using the *gll_iem_v02* map cube, and the extragalactic emission and the residual instrumental backgrounds were modeled jointly using the *iso_p7v6source* template². The spectral model used in this analysis also included the contributions of 2FGL sources (13) within 20° of the center of the field of view, and the contribution from the pulsar was modeled using an exponentially cut-off power-law (ECPL) of the form $dN/dE \propto E^{-\Gamma} \exp(-E/E_c)$ where E represents the photon energy, Γ is the photon index and E_c is the cutoff energy of the spectrum. The normalizations of the diffuse components were left free in the fit, as well as spectral

¹<http://fermi.gsfc.nasa.gov/ssc/data/analysis/scitools/overview.html>

² <http://fermi.gsfc.nasa.gov/ssc/data/access/lat/BackgroundModels.html>

parameters of sources within 8° of the pulsar sky position. The best-fit spectral parameters for PSR J1311–3430 along with the derived photon and energy fluxes are displayed in Table 1 and characterize the pulse-phase-averaged gamma-ray spectrum of the pulsar (Fig. S1). The measured energy flux is consistent with that published earlier for this gamma-ray source (13). We checked the best-fit parameters listed in Table 1 with the `pointlike` likelihood analysis tool (23), and found results that are consistent within uncertainties. The tool `gtsrcprob` and the spectral model obtained from the likelihood analysis were finally used to calculate the probabilities that the photons originate from PSR J1311–3430.

We also performed a spectral analysis resolved in pulse phase (rotational phase) for PSR J1311–3430. For this, we divided the data set into ten segments according to pulse phase and measured the gamma-ray spectrum in each of those segments in a binned likelihood analysis assuming an ECPL model for the pulsar (Fig. S2). As observed for other bright gamma-ray pulsars [e.g. (36)], the spectral properties of PSR J1311–3430 evolve strongly with rotational phase, suggesting varying emission altitudes and curvature radii of the magnetic field lines. In addition, significant gamma-ray emission is detected over all rotational phases: selecting phases between 0.8 and 1.2 we measured a photon flux for PSR J1311–3430 of $(4.6 \pm 0.9) \times 10^{-8}$ photons $\text{cm}^{-2} \text{s}^{-1}$, and a photon flux of $(2.8 \pm 1.6) \times 10^{-8}$ photons $\text{cm}^{-2} \text{s}^{-1}$ for pulse phases between 0.9 and 1.1. In the former phase interval, the exponentially cut-off power-law model is preferred over a simple power-law spectral shape at the $\sim 3.5\sigma$ significance level, and at $\sim 2.5\sigma$ for the latter phase interval. This potentially indicates a magnetospheric origin for this “off-pulse” emission. The existence of magnetospheric emission in the off-pulse region of the gamma-ray pulse profiles is predicted from theoretical models under specific geometrical orientations (37) and can give insights into the pulsar emission geometry.

We also conducted an analysis to look for an orbital modulation of the gamma-ray flux and the spectrum. We subdivided the orbit into ten equally spaced bins, and for each subset of data

we performed a binned likelihood analysis. The flux, the spectral index Γ , and the energy cut-off E_c are compatible with a constant value all along the orbit. Thus, we proceeded to compute the formal 95% confidence upper limits on the amplitude of a sinusoidal modulation and obtained $< 2.6 \times 10^{-8}$ photons $\text{cm}^{-2} \text{s}^{-1}$ for the flux, < 0.32 for Γ , and < 2.2 GeV for E_c .

Pulsar search in LAT data

To correct for the Doppler modulation due to the satellite's motion in the Solar System, we applied barycenter corrections to the arrival times of the LAT gamma-ray photons using the JPL DE405 Solar System ephemeris.

Constructing the parameter-space grid for the semi-coherent search (the first stage of the hierarchical search scheme) as efficiently as possible is of utmost importance, because this stage dominates the overall computing cost. For this purpose, we developed an algorithm that effectively utilizes the metric formalism. The metric provides a geometric tool measuring the expected fractional loss in squared signal-to-noise ratio for any given pulsar-signal location at a nearby grid point. The metric components along the search-space directions of f and \dot{f} are constant across the entire space [see, e.g., (18, 19)]. In contrast, the orbital metric components (in search-space directions of $\{P_{\text{orb}}, T_{\text{asc}}, x\}$) explicitly depend upon the search parameters [see, e.g., (24)]. This implies that the metric (and so the grid-point density required to not miss a signal) changes across orbital parameter space. Therefore, constructing a simple lattice with constant spacings over these dimensions would be highly inefficient, resulting in either vast over- or under-covering of large parameter-space regions.

In contrast, the grid-construction algorithm we developed follows a more efficient approach. While using constant spacings in f and \dot{f} , grid points over $\{P_{\text{orb}}, T_{\text{asc}}, x\}$ are first placed at random [e.g., (38)]. Then those that are either too close together or too far apart according to the metric are moved (barycentric shifts), minimizing the maximum possible loss in signal-to-noise

ratio for any pulsar signal across the entire search parameter space. To accelerate this otherwise computationally-bound process, we divided the search space into sub-volumes to avoid metric distance comparisons between a trial point and *every* other grid point, exploiting an efficient hashing technique. For an arbitrary point in parameter space, the index of the enclosing sub-volume (and thus the parameters of its neighboring points) is obtained from a hash table through a fast rounding operation. By design the resulting grid ensured never losing more than 30% of the signal-to-noise ratio for any signal parameters. Finally, we used simulated pulsar signals to validate this design goal. This process is also highly accelerated by exploiting the hash table, because it provides quick access to the closest grid points around any given parameter-space location. This way, the search for each simulated pulsar signal is computationally inexpensive, because only the relevant subset of nearest grid points around each signal are searched.

In the blind search, we obtained the semi-coherent detection statistic (coherent Fourier power) computed using a coherence window of $T = 2^{20}$ s (~ 12 days) being incoherently combined by sliding the window over the entire 4 years of LAT data) over the entire f grid by exploiting the efficiency of the fast Fourier transform (FFT) algorithm. For this purpose, we divided total f search range into separate bands using a heterodyning bandwidth of $\Delta f_{\text{BW}} = 128$ Hz. Thus, the FFT contains $T \Delta f_{\text{BW}} \cong 10^8$ frequency bins. This choice for Δf_{BW} allowed us to fit the computation into memory on the ATLAS computing cluster to maximize performance. In the \dot{f} direction, we analyzed about 10^2 uniformly spaced grid points. The use of separate frequency bands is also extremely advantageous in view of the orbital grids, which we adapted to each band. This further reduced the computational cost, since the total number of required grid points to cover the orbital parameter space $\{P_{\text{orb}}, T_{\text{asc}}, x\}$ is about $10^7 (f_{\text{max}}/700 \text{ Hz})^3$ and increases with f_{max} cubed, where f_{max} is the highest spin frequency (most conservative choice) in the search band (before heterodyning). Thus, in total the search grid covering the frequency band near 700 Hz comprised about $10^8 \times 10^2 \times 10^7 = 10^{17}$ points.

We note that the heterodyning step reduces the bandwidth of the data to 128 Hz, which is still much larger than the narrow bandwidth of the signal (that is about $f \times 10^{-4}$, which is ~ 0.04 Hz for PSR J1311–3430) that remains unaffected by this. The heterodyning does not alter the pulsar signal shape (i.e., the extension in parameter space) - it is merely shifted in the frequency domain and so the metric is unaffected and still depends on f_{max} , the original upper frequency. This f_{max}^3 -dependency is readily seen from the fact that the amplitude of the pulsar-rotational-phase modulation due to the binary motion is proportional to the spin frequency f . And, the metric components involve products of first-order derivatives of the rotational phase with respect to the parameters (*17–19, 24*). As the number of grid points is proportional to the square root of the metric determinant, it therefore increases with f^3 (one f contribution from each of the three orbital dimensions searched).

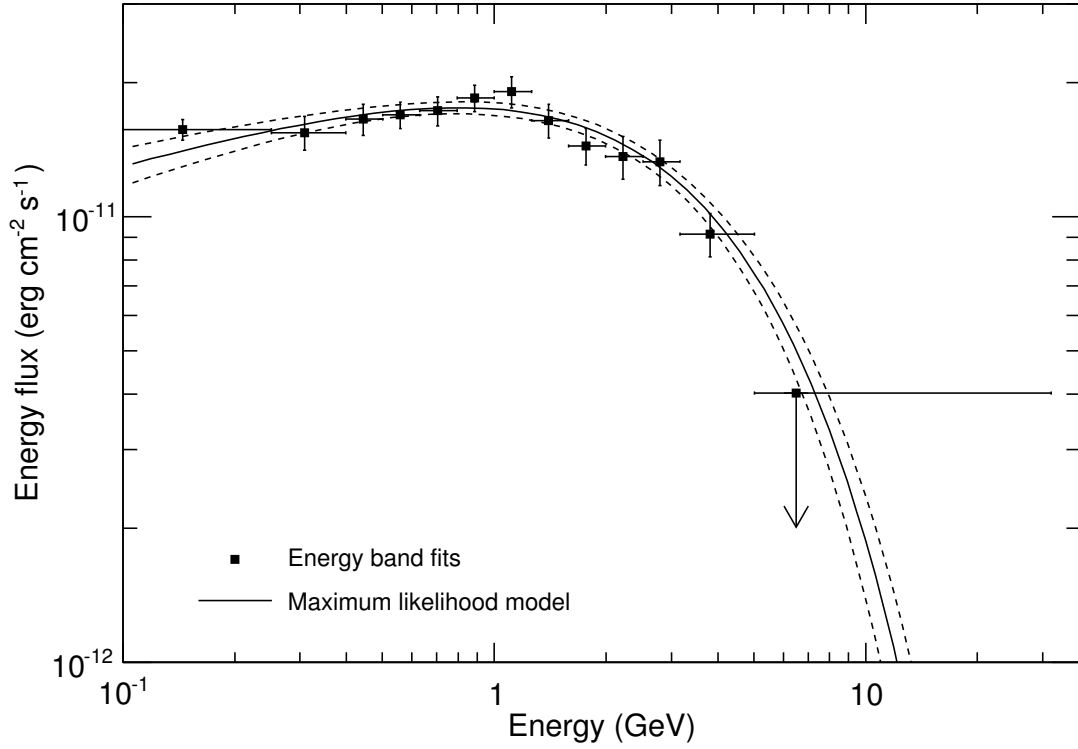


Fig. S1. Pulse-phase-averaged gamma-ray spectral energy distribution for PSR J1311–3430. Data points (solid squares) are derived from fits of individual energy bands with variable widths, in which the pulsar is detected with a significance greater than 15σ . In these individual bands the pulsar emission is modeled with a simple power-law spectrum. We calculated an upper limit for the highest energy band, in which the pulsar was not detected with sufficient significance. The solid curves represents the best-fit model obtained from the likelihood analysis and dashed curves indicate the 1σ uncertainties.

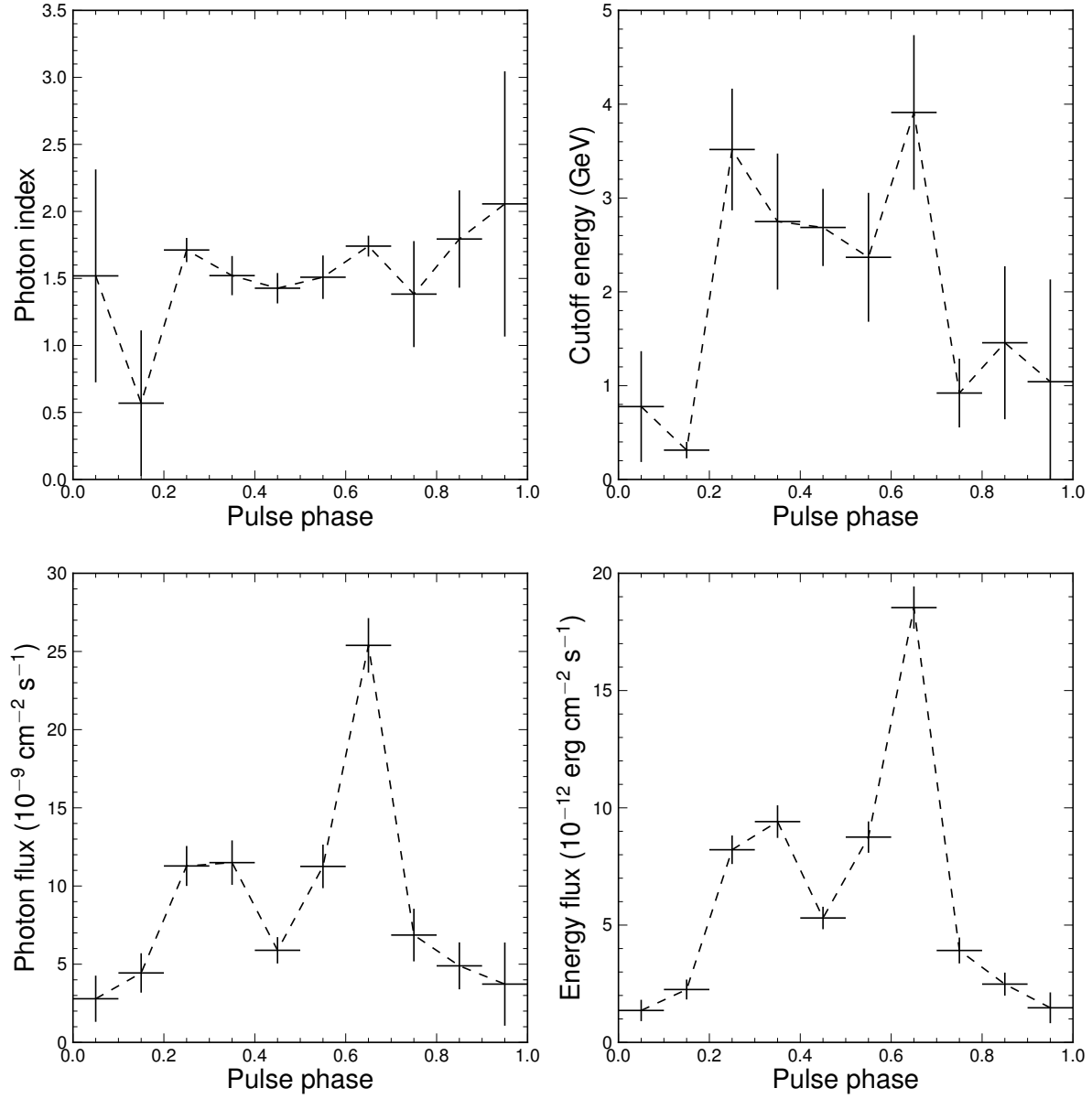


Fig. S2. Pulse-phase-resolved gamma-ray spectral analysis for PSR J1311–3430 using 10 bins per rotation. The different panels show the photon index (**top left**), cutoff energy (**top right**), photon flux above 0.1 GeV (**bottom left**), and energy flux above 0.1 GeV (**bottom right**). Error bars indicate statistical 1σ uncertainties.